

3D image-domain wavefield tomography using time-lag extended images

Tongning Yang and Paul Sava

Center for Wave Phenomena, Colorado School of Mines

ABSTRACT

Image-domain wavefield tomography is a technique that reconstructs the velocity model by extracting information from migrated images. In time-lag extended images, velocity model accuracy can be evaluated by reflection focusing error, which represents the traveltimes residual in the image domain. The model is updated by minimizing an objective function similar to the one used by wave-equation traveltimes inversion. Unlike wave-equation traveltimes inversion wherein traveltimes residual is obtained from crosscorrelation of a single-shot data, the focusing error is extracted from time-lag gathers, which are wavefield crosscorrelations based on multiple experiments. Because the signal-to-noise ratio is higher in common-image gathers than that in common-shot gathers, our technique is able to measure focusing error more accurately in presence of noisy data and complex geologic structures. In addition, the image-domain approach is robust as it does not suffer from cycle-skipping, which is common in conventional data-domain full-waveform inversion. We also use the focusing error to precondition the gradient of the objective function in order to improve the convergence of the inversion. This is done by constructing a gradient mask which restricts the model updates to areas where the accumulated focusing error exceeds a certain threshold. This preconditioning of the gradient limits the model update to areas containing the velocity model errors. We illustrate the method using both synthetic and field data. The North Sea 3D field data example demonstrates that the technique is effective in optimizing the velocity model and improving image quality. In addition, the method is efficient in 3D because only the time-lag extensions are computed and stored, in contrast to differential semblance optimization which requires costlier inline and crossline space-lag extensions.

Key words: wavefield tomography, 3D, extended images, adjoint-state method, focusing error

1 INTRODUCTION

In seismic imaging, building an accurate and reliable velocity model remains one of the biggest challenges. The need for high-quality velocity models is driven by the wide-spread use of advanced imaging techniques such as one-way wave-equation migration (WEM) and reverse-time migration (RTM) (Etgen et al., 2009).

In the past decade, velocity model-building methods using full seismic wavefields (Tarantola, 1984; Pratt, 1999; Vigh and Starr, 2008; Symes, 2009) have become popular mainly because of their accuracy and because the availability of increased computational power. One can divide the family of such velocity-estimation techniques into data-domain meth-

ods (Sirgue and Pratt, 2004; Plessix, 2009) and image-domain methods (Sava and Biondi, 2004; Shen and Symes, 2008; Yang and Sava, 2011). Data-domain methods adjust the velocity model by minimizing the difference between simulated and recorded data (Tarantola, 1984; Pratt, 1999). This formulation is based on the strong assumption that the wave equation used for data simulation is consistent with the physics of the earth, which is often violated in practice. In addition, the methods also require low-frequency data and sufficiently accurate initial model to avoid the cycle-skipping problem.

Unlike the data-domain approaches, image-domain methods update the velocity model by optimizing the image quality. As stated by the semblance principle (Al-Yahya, 1989;

Yilmaz, 2001), the image obtained by multiple and redundant seismic experiments is optimized when the correct velocity model is used to migrate the data. The common practice is to optimize image coherency in common-image gathers by iteratively updating the velocity model. In complex geology, image-domain wavefield tomography is capable of handling complicated wave propagation because it uses a wave-equation engine to simulate the wavefields. Furthermore, the band-limited wavefields used in the velocity model building are consistent with the wave-equation migration algorithms used in imaging.

The cycle-skipping problem in conventional data-domain full-waveform inversion is mainly caused by its objective function, which is the L-2 norm of the difference between the observed and simulated data. Cycle-skipping occurs when the initial model is not accurate enough or the data do not have sufficiently low frequency components. To overcome this problem, wave-equation traveltime inversion was proposed to reconstruct the velocity model in complex geologic environments (Luo and Schuster, 1991; Zhang and Wang, 2009; van Leeuwen and Mulder, 2010). The essential idea behind this method is to invert the velocity model using only the traveltime information rather than full waveforms. In this way, the nonlinearity of the objective function with respect to the model is significantly reduced, and the objective function is less sensitive to data noise and the accuracy of the initial model. For wave-equation traveltime inversion, the traveltime residual is obtained from the cross-correlation between the recorded and simulated data, and then spread along the wavepath computed by solving the wave equation in the background model. Nonetheless, these techniques aim to invert for a velocity model using transmission waves, and not reflected waves. As a result, they are limited to cross-well experiments or to surface experiments with diving waves.

Velocity model updates using traveltime residuals are also performed in the image domain, by techniques known as *focusing analysis* (Faye and Jeannot, 1986). The traveltime residual is defined as *focusing error*, since it uses the focusing of reflections as a measure for the coherence of migrated images. Such information indicates the accuracy of the velocity model and thus can be used for model building. For wave-equation migration, one can extract focusing information from time-lag extended images (Sava and Fomel, 2006); focusing is quantified as the reflection focus shift along the time-lag axis. Wang et al. (2005) propose a velocity analysis method using time focusing applied to re-datumed data sets. Their approach is ray-based and thus may become unstable when the complex geology results in multi-pathing. Higginbotham and Brown (2008) and Brown et al. (2008) also propose a model-building method that converts the focusing error into velocity updates using an analytic formula. However, the formula is derived under the 1D assumption, the focusing error is transformed into vertical updates only, and therefore the accuracy of the method is degraded in areas with strong lateral velocity variations. Wang et al. (2008, 2009) illustrate that focusing analysis can be used as an image-enhancement tool to improve the image quality and to update subsalt velocity models. Yang

and Sava (2010a) analyze the relationship between the focusing error and velocity model accuracy, and develop a wave-equation migration velocity analysis based on this relationship (Yang and Sava, 2010b).

Here, we propose a methodology for 3D image-domain tomography using the focusing information of migrated images. The essential idea is to extract focusing error from time-lag extended images and then convert it into velocity updates by a procedure similar to wave-equation traveltime inversion (Luo and Schuster, 1991). In addition, we use focusing error to constrain the updates only in target areas where velocity error exists and to speed up the convergence of the inversion. We begin by defining an objective function based on measured image focusing. We discuss its gradient computation and illustrate how the focusing error can be used to construct a mask for preconditioning the gradient. Then we use a simple synthetic model to illustrate the workflow of the method and present an application of the method to a North Sea 3D OBC field dataset. The improved image quality and flatter events in angle-domain common-image gathers demonstrate that the method is a robust and effective 3D velocity model-building tool. Finally, we compare and contrast our approach to other wave-equation-based velocity model building methods.

2 THEORY

The objective function for our wavefield tomography approach is

$$J = \frac{1}{2} \|\Delta\tau\|^2. \quad (1)$$

Here $\Delta\tau$ stands for the focusing error, which is the time lag of reflection focus away from zero measured in extended images. Time-lag extended images are the crosscorrelation between extrapolated wavefields (u_s and u_r)

$$R(\mathbf{x}, \tau) = \sum_j \sum_{\omega} \overline{u_s(j, \mathbf{x}, \omega)} u_r(j, \mathbf{x}, \omega) e^{-2i\omega\tau}, \quad (2)$$

where j is the shot index, ω is the angular frequency, and \mathbf{x} are the space coordinates $\{x, y, z\}$. The source and receiver wavefields u_s and u_r satisfy

$$\begin{bmatrix} \mathcal{L}(\mathbf{x}, \omega, m) & 0 \\ 0 & \mathcal{L}^*(\mathbf{x}, \omega, m) \end{bmatrix} \begin{bmatrix} u_s(j, \mathbf{x}, \omega) \\ u_r(j, \mathbf{x}, \omega) \end{bmatrix} = \begin{bmatrix} f_s(j, \mathbf{x}, \omega) \\ f_r(j, \mathbf{x}, \omega) \end{bmatrix}, \quad (3)$$

where \mathcal{L} and \mathcal{L}^* are forward and adjoint frequency-domain wave operators, and f_s and f_r are the source and receiver data. The wave operator \mathcal{L} and its adjoint \mathcal{L}^* propagate the wavefields forward and backward in time, respectively, using a two-way wave equation, i.e., $\mathcal{L} = -\omega^2 m - \Delta$, where m represent slowness squared and Δ is the Laplacian operator.

The objective function in equation 1 is the same as that defined in wave-equation traveltime inversion (Luo and Schuster, 1991; Zhang and Wang, 2009). However, the physical meanings of $\Delta\tau$ in the objective functions differ. In our approach, $\Delta\tau$ is the focusing error measured from the stack over shots of image obtained by wavefield crosscorrelation. In contrast, $\Delta\tau$ in wave-equation traveltime inversion is the travel-

time misfit measured between observed and simulated data at the known receiver locations for a single shot.

We compute the gradient of our objective function using the adjoint-state method (Plessix, 2006). The first step is to construct state variables u_s and u_r , which relate the objective function to the model parameters (equation 3). The next step is to construct the adjoint sources, which are used to obtain adjoint-state variables. The adjoint sources are the derivative of the objective function with respect to the state variables. In our case, as $\Delta\tau$ is not directly dependent on the wavefields, we use the *connective function* similar to the one developed by Luo and Schuster (1991). Since the focusing error represents the time lag when the reflection events focus, we have

$$R(\mathbf{x}, \Delta\tau) = \max\{R(\mathbf{x}, \tau) \mid \tau \in [-T, T]\}. \quad (4)$$

As a result, the connective function can be written as

$$\begin{aligned} \dot{R}_{\Delta\tau} &= \left. \frac{\partial R}{\partial \tau} \right|_{\Delta\tau} \\ &= \sum_j \sum_{\omega} (-2i\omega) \overline{u_s(j, \mathbf{x}, \omega)} u_r(j, \mathbf{x}, \omega) e^{-2i\omega\Delta\tau}. \end{aligned} \quad (5)$$

The adjoint sources are then obtained as

$$g_s(j, \mathbf{x}, \omega) = \frac{\partial J}{\partial (u_s)} = \Delta\tau \frac{\partial(\Delta\tau)}{\partial (u_s)} = \Delta\tau \frac{\frac{\partial(\dot{R}_{\Delta\tau})}{\partial (u_s)}}{\frac{\partial(\dot{R}_{\Delta\tau})}{\partial (\Delta\tau)}} \quad (7)$$

$$= \frac{\Delta\tau}{E} (2i\omega) \overline{u_r(j, \mathbf{x}, \omega)} e^{2i\omega\Delta\tau} \quad (8)$$

and

$$g_r(j, \mathbf{x}, \omega) = \frac{\partial J}{\partial (u_r)} = \Delta\tau \frac{\partial(\Delta\tau)}{\partial (u_r)} = \Delta\tau \frac{\frac{\partial(\dot{R}_{\Delta\tau})}{\partial (u_r)}}{\frac{\partial(\dot{R}_{\Delta\tau})}{\partial (\Delta\tau)}} \quad (9)$$

$$= \frac{\Delta\tau}{E} (-2i\omega) u_s(j, \mathbf{x}, \omega) e^{-2i\omega\Delta\tau}, \quad (10)$$

where

$$E = \sum_j \sum_{\omega} 4\omega^2 \overline{u_s(j, \mathbf{x}, \omega)} u_r(j, \mathbf{x}, \omega) e^{-2i\omega\Delta\tau}. \quad (11)$$

The adjoint-state variables are constructed similarly to state variables as follows:

$$\begin{bmatrix} \mathcal{L}^*(\mathbf{x}, \omega, m) & 0 \\ 0 & \mathcal{L}(\mathbf{x}, \omega, m) \end{bmatrix} \begin{bmatrix} a_s(j, \mathbf{x}, \omega) \\ a_r(j, \mathbf{x}, \omega) \end{bmatrix} = \begin{bmatrix} g_s(j, \mathbf{x}, \omega) \\ g_r(j, \mathbf{x}, \omega) \end{bmatrix}. \quad (12)$$

The gradient of the objective function is simply the crosscorrelation between state and adjoint-state variables:

$$\frac{\partial J}{\partial m} = \quad (13)$$

$$\sum_j \sum_{\omega} \frac{\partial \mathcal{L}}{\partial m} \left(u_s(j, \mathbf{x}, \omega) \overline{a_s(j, \mathbf{x}, \omega)} + u_r(j, \mathbf{x}, \omega) \overline{a_r(j, \mathbf{x}, \omega)} \right), \quad (14)$$

where $\frac{\partial \mathcal{L}}{\partial m}$ is just $-\omega^2$.

One common problem for image-domain wavefield tomography is that the computed gradient always distributes the

measured misfit along the wavepaths from image points to the surface. This is because the focusing error actually measures velocity model error accumulated from top to bottom, and the gradient spreads the updates all the way up to the surface. If certain areas above the image point do not contain error in the velocity model, the inversion needs additional iterations to eliminate the update in this region, which consequently slows the convergence of the inversion. To ameliorate this problem, we use the focusing error as a constraint for the inversion. The focusing error is associated with the accuracy of the velocity model and accumulated from top to bottom in a way similar to the velocity model error. Therefore, the integral of the focusing error absolute value over depth indicates the distribution of the velocity model error. If this integral in a certain area is close to zero, then the velocity model for this area and above is accurate and needs no updates. Therefore, we can construct a gradient mask to mute areas where no model update is required. We define the gradient mask W as:

$$W(\mathbf{x}) = \begin{cases} 0 & \text{if } \int_0^z |\Delta\tau(x, y, z)| dz < \tau_0 \\ 1 & \text{elsewhere} \end{cases}, \quad (15)$$

where τ_0 is a user-defined threshold. By applying the gradient mask and limiting the model updates in the target regions, we reduce the number of iterations needed by the inversion and improve the convergence of the method. This idea is similar to applying layer-stripping in velocity model building: we first update the model in the shallow regions, and then proceed to updates of the deeper portion of the model while keeping the upper portion fixed.

3 EXAMPLES

We demonstrate the gradient computation and preconditioning of our method using a synthetic horizontally layered model, and then we apply the method to a North Sea 3D OBC field dataset.

Figure 1(a) shows the velocity profile of the synthetic model. The model has two interfaces located at $z = 0.5$ km and $z = 1.1$ km, and the velocities for the three layers from top to bottom are 1.5, 1.7, and 2.3 km/s. We simulate the data using acoustic two-way wave-equation finite-difference modeling. The initial model used for imaging is constant using the velocity from the first layer in the true model, i.e. 1.5 km/s. We use this model to migrate the data and to obtain the image and the time-lag gathers. As the initial model is correct in the first layer, we expect that the first interface be correctly imaged, and the second interface shifted. The migrated image in Figure 1(b) indeed shows that the first reflector is correctly imaged at $z = 0.5$ km, and that the second reflector is too shallow, at $z = 1.0$ km. Figure 2 shows a gather located at the center of the model. Using such gathers, we can extract the focusing error $\Delta\tau$ by measuring the lag of the focus from zero time lag. Here, the time-lag gathers accurately capture the velocity information: as there is no velocity model error associated with the first layer, the corresponding reflection focus is

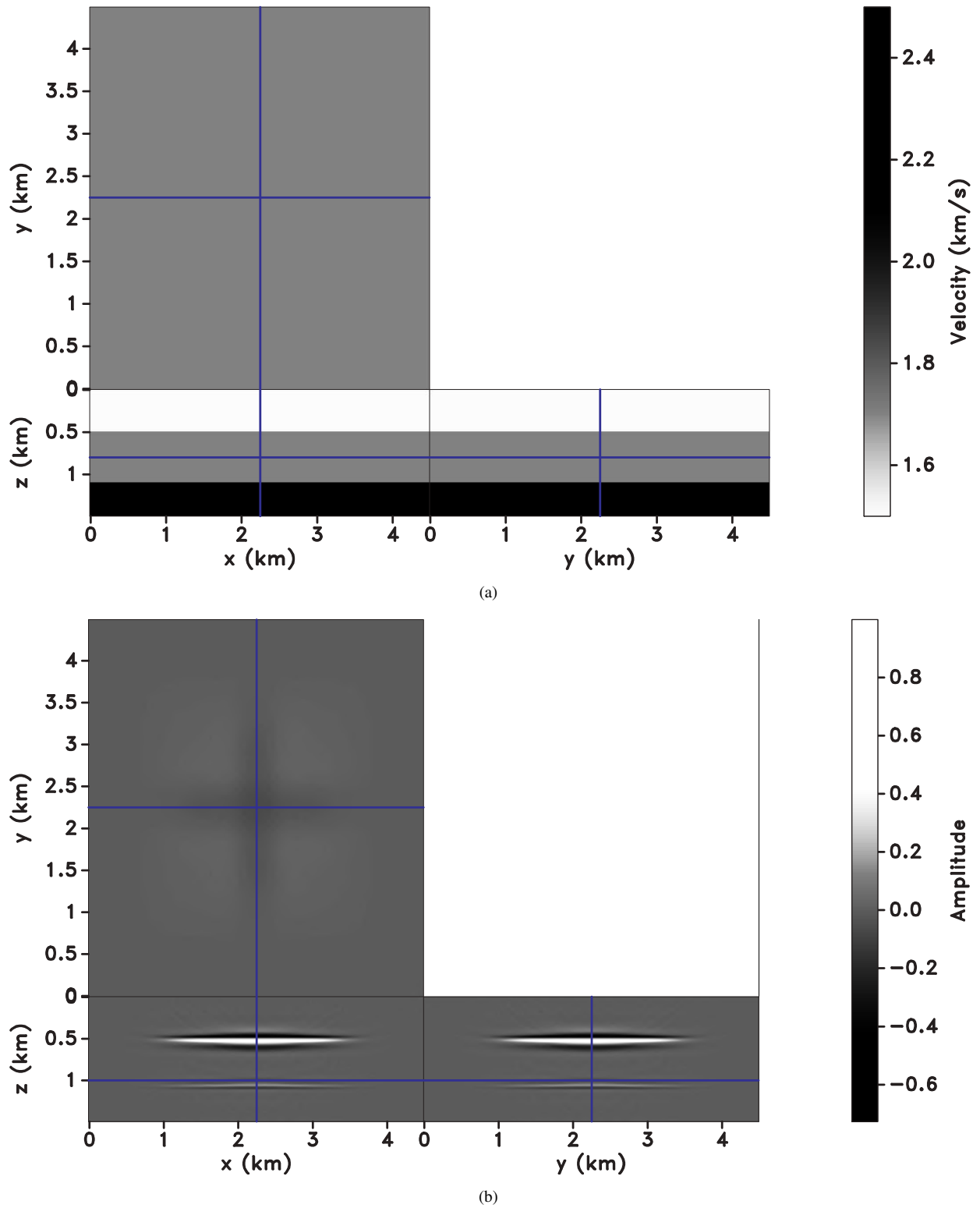


Figure 1. (a) The layered velocity model, and (b) migrated image obtained with the initial model, the constant with velocity from the first layer in the true model, i.e. 1.5 km/s.

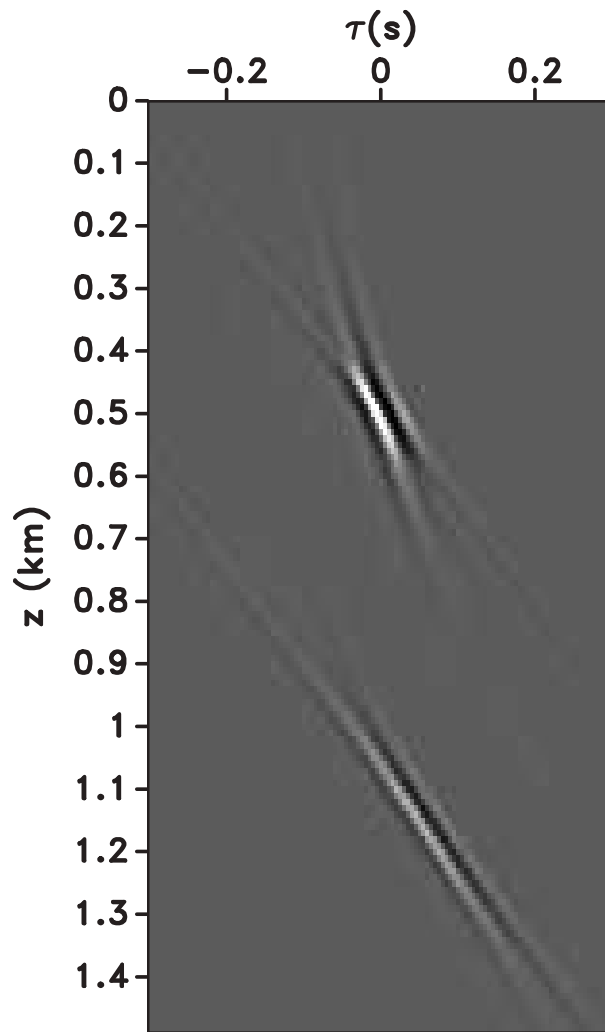
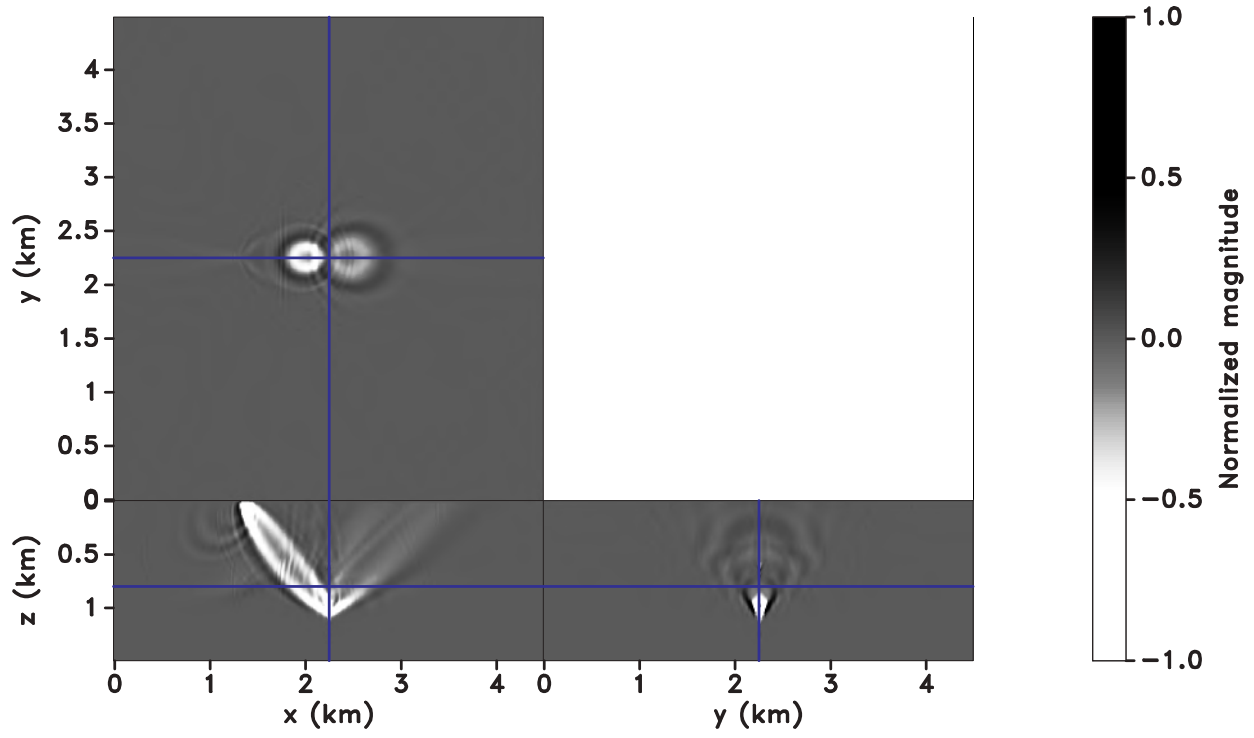
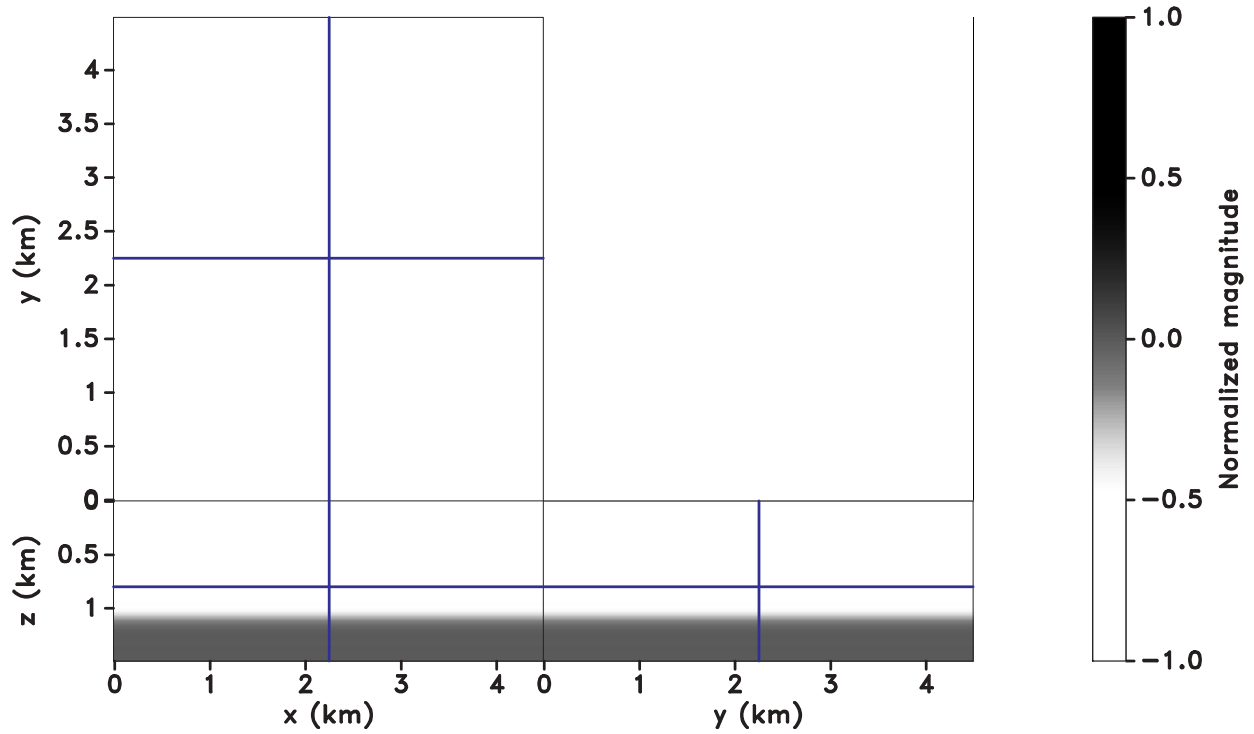


Figure 2. Time-lag gathers obtained with the initial model. The gather is located at $x = 2.25$ km, $y = 2.25$ km. The reflection focus of the top layer is located at zero lag as there is no velocity error. The focus of the second layer shifts to positive 0.1 s due to the incorrect initial model.

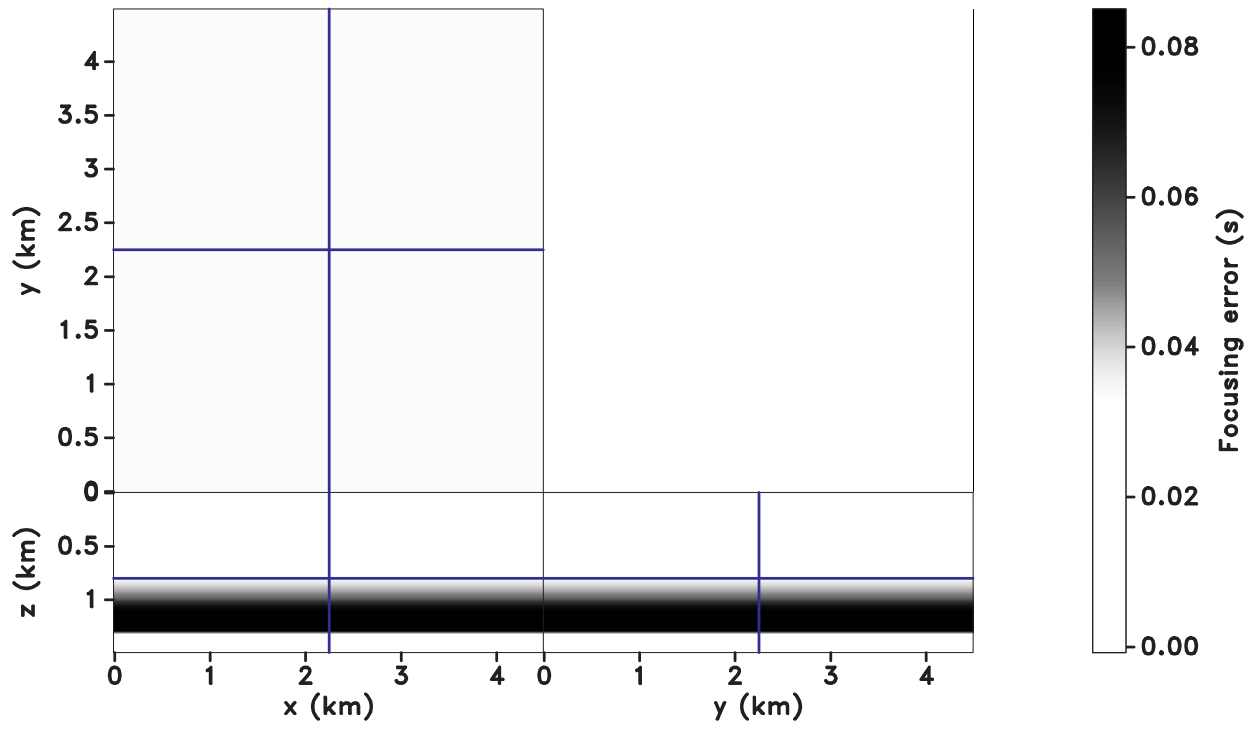


(a)

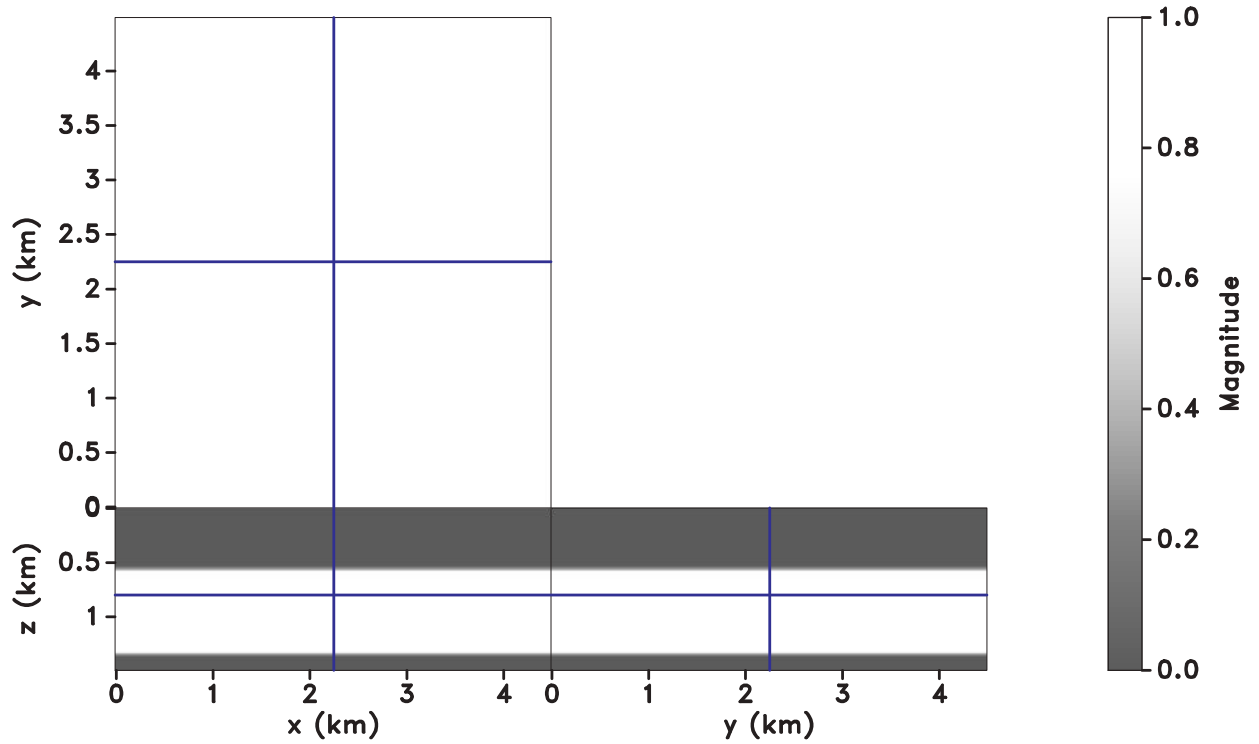


(b)

Figure 3. (a) The gradient obtained with a single shot, which corresponds to the sensitivity kernel of our method, and (b) the gradient obtained with all shots.

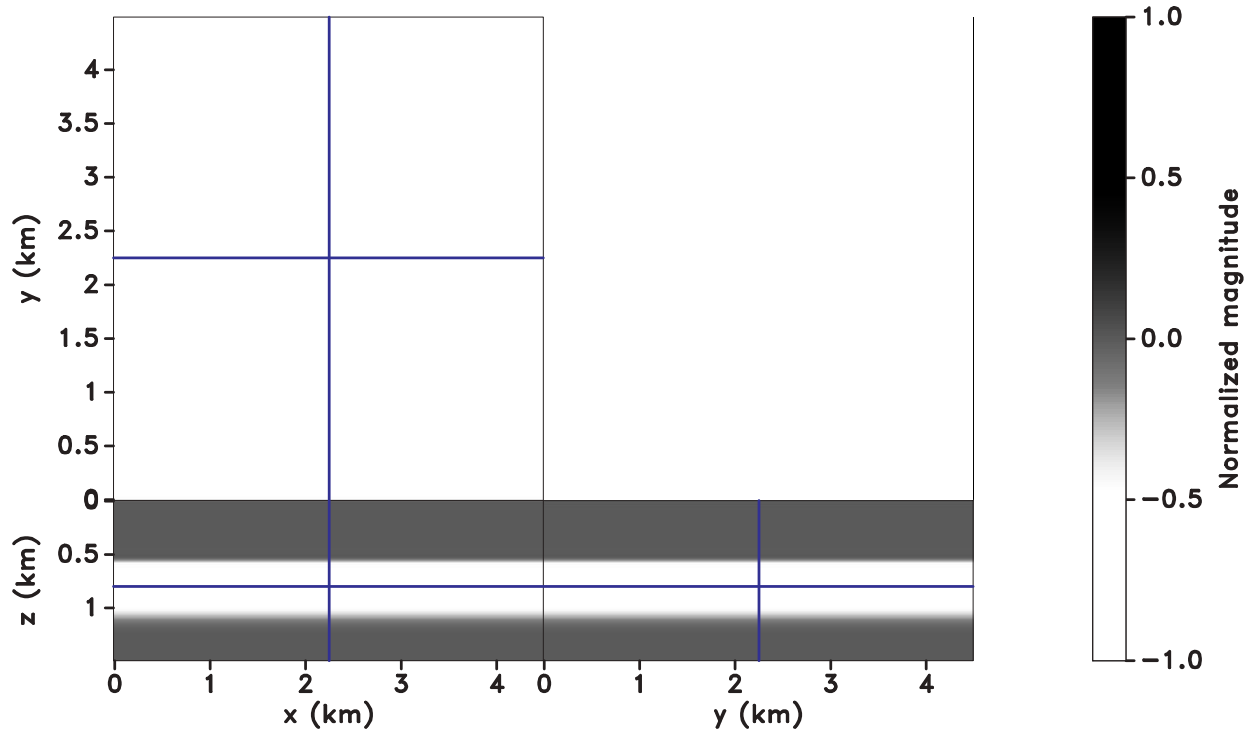


(a)

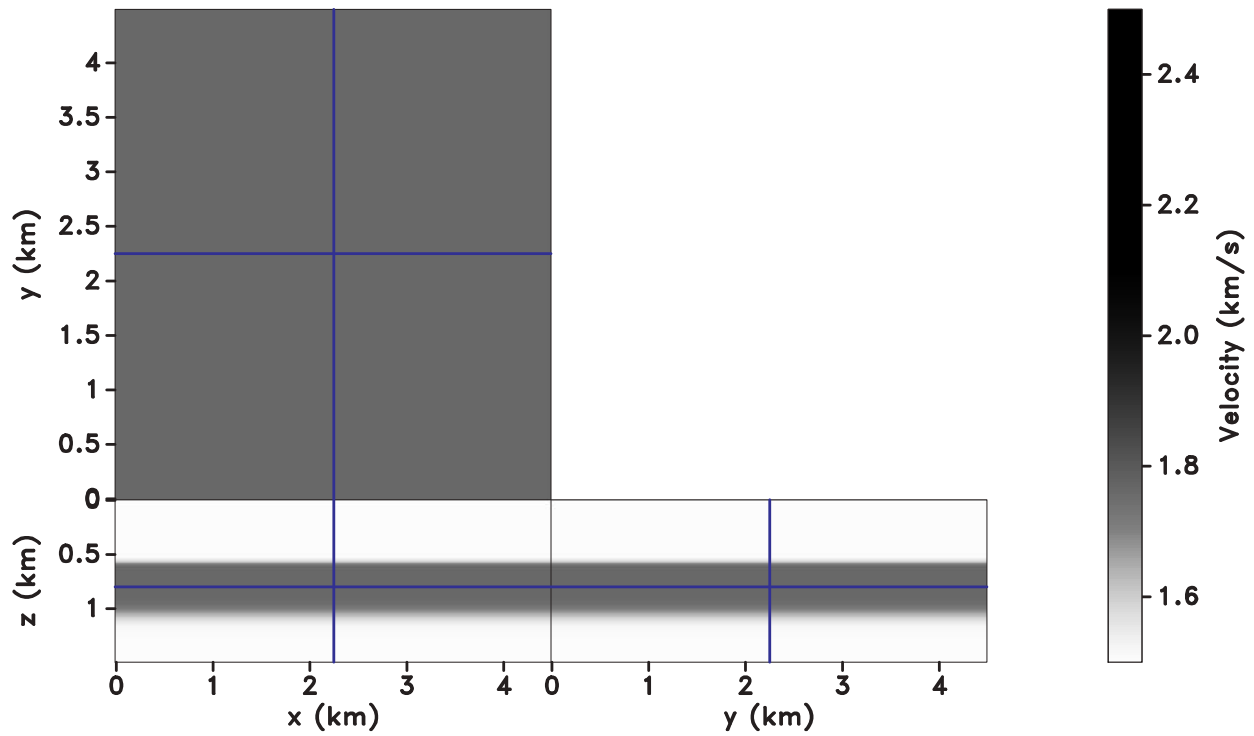


(b)

Figure 4. (a) The focusing error extracted from the time-lag gathers. (b) The gradient mask obtained using equation 11.



(a)



(b)

Figure 5. (a) The gradient obtained after applying the mask. (b) The updated model using the gradient in (a) after one iteration.

located at zero time lag. In contrast, the reflection focus of second layer is shifted to $\tau = 0.1$ s indicating that the migration velocity is lower than that of the true model. Using the focusing error, we construct the objective function and compute the gradient following the workflow discussed in the previous section. Figure 3(a) plots the gradient obtained for one gather at the center of the model and one shot located at $x = 1.1$ km, $y = 2.25$ km. This single-shot gradient corresponds to the sensitivity kernel of the method. The kernels connecting the source and receivers to the image point on the second layer. Figure 3(b) plots the gradient obtained for all gathers and all shots. The gradient is negative, indicating that the velocity of the initial model should be increased, which agrees with our experimental setup. The gradient in Figure 3(b) also suggests an update in the area between $z = 0$ km and $z = 0.5$ km, because the sensitivity kernels for the second layer distribute the focusing error along the path from the source to image points to receivers. However, the focusing error (Figure 4(a)), which characterizes the velocity model error distribution, is zero in the top layer because there is no velocity error in this area. This demonstrates that the computed gradient is not consistent with the velocity error distribution, so we need to restrict the updates from the top layer. Using the focusing error as a priori information, we construct the gradient mask using equation 15, as shown in Figure 4(b). Because the mask is zero in the first layer, this effectively removes the updates there. The final preconditioned gradient, after applying the mask, is plotted in Figure 5(a). The update is now limited to the second layer only, and results in a faster convergence for the inversion. In this simple case, we reconstruct the model shown in Figure 5(b) after only one iteration.

The North Sea 3D OBC field dataset was acquired in the Volve field, and the construction of the initial model is described in Szydlík et al. (2007). The Earth model is anisotropic and can be described using the Thomsen parameters V_p , ϵ , and δ (Thomsen, 1986). Here we assume that the medium is isotropic and use only the V_p model to test our algorithm. Figures 6(a) and 7(a) show the initial model obtained by a layer-stripping method and the corresponding migrated image. Using the objective function and gradient computation discussed in the previous section, we run the inversion for five iterations. The updated velocity model and its corresponding migrated image are plotted in Figures 6(b) and 7(b). Observe that the inversion increases the velocity around the center part of the model between $z = 2.5$ km-4.0 km. This update improves the image quality, as the main reflections around $z = 2.8$ km are more focused and coherent, and the continuity of the deeper reflections improves as well. These improvements can be better observed in the zoom-in inline sections extracted at $y = 3.5$ km in Figures 8(a) and 8(b). To further assess the model improvement, we construct angle-domain common-image gathers before and after the inversion. Figures 9(a)-9(c) and Figures 10(a)-10(c) plot angle gathers sampled in the inline direction at three different crossline locations using the initial and updated models, respectively. Notice that the main reflector around $z = 2.8$ km is characterized

by flatter gathers after the inversion, indicating the model improvement.

4 DISCUSSION

We demonstrate an image-domain wavefield tomography approach that can be used as an alternative to data-domain wave-equation traveltimes inversion. We use focusing to measure a traveltimes error, which depends on the velocity model error, i.e., we formulate an objective function by minimizing the focusing error.

Our method shares many similarities with wave-equation traveltimes inversion, e.g., the objective function construction. The main difference between these two techniques, however, lies in how the focusing information is extracted. In wave-equation traveltimes inversion, the traveltimes residual $\Delta\tau$ is obtained from the cross-correlation between recorded and simulated data in individual shot gathers. In contrast, our method estimates the focusing error $\Delta\tau$ from time-lag gathers, which are the cross-correlations of extrapolated source and receiver wavefields stacked over all experiments. In general, the signal-to-noise ratio in common-image gathers is higher than in shot gathers due to the stacking process. Thus, the approach proposed here is expected to render more accurate focusing information in presence of noise and complex geology. Besides, wave-equation traveltimes inversion is designed to extract the traveltimes information from transmission waves, which can be used only in cross-well geometry or for diving waves in surface acquisition. Our approach, in contrast, extracts the traveltimes information from reflected waves, and thus it is capable of inverting the velocity model in deeper target regions.

Furthermore, our method requires less computational efforts compared to differential semblance optimization (DSO). DSO uses space-lag gathers and needs to compute the lags in both inline and crossline directions in 3D. This leads to 5D image hypercubes which are too expensive to compute and store. In comparison, our method requires only the time lag to evaluate velocity information even in 3D. As a result, the computational and storage cost is at least one order of magnitude lower than in the case of space-lag gathers. Nonetheless, the azimuthal resolution of our method is lower than that provided by DSO since the time-lag itself is not sufficient to characterize the azimuth information in the gathers.

5 CONCLUSION

We develop a 3D image-domain velocity model building technique based on time-lag extended images, which characterize the traveltimes residual due to velocity error by reflection focusing. We formulate the optimization problem by minimizing the focusing error based on images constructed by wave-equation migration, which puts our technique in the family of wavefield tomography techniques. We speed up inversion by exploiting focusing information as a priori information to precondition the gradient. A North Sea field data example illustrates that our method is effective in improving model accu-

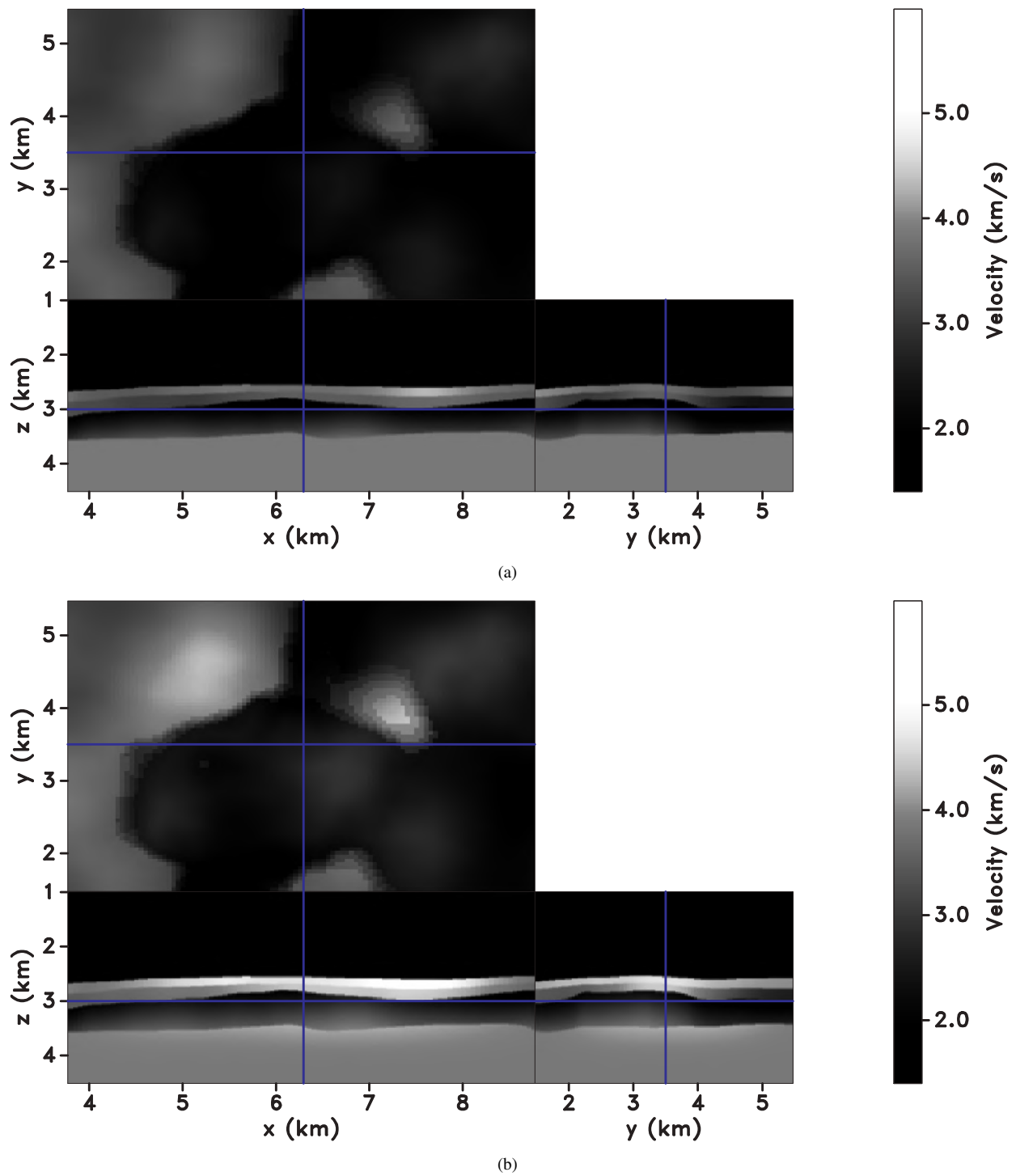


Figure 6. North Sea field data example. (a) The initial model used for the inversion, and (b) the updated model obtained after the inversion.

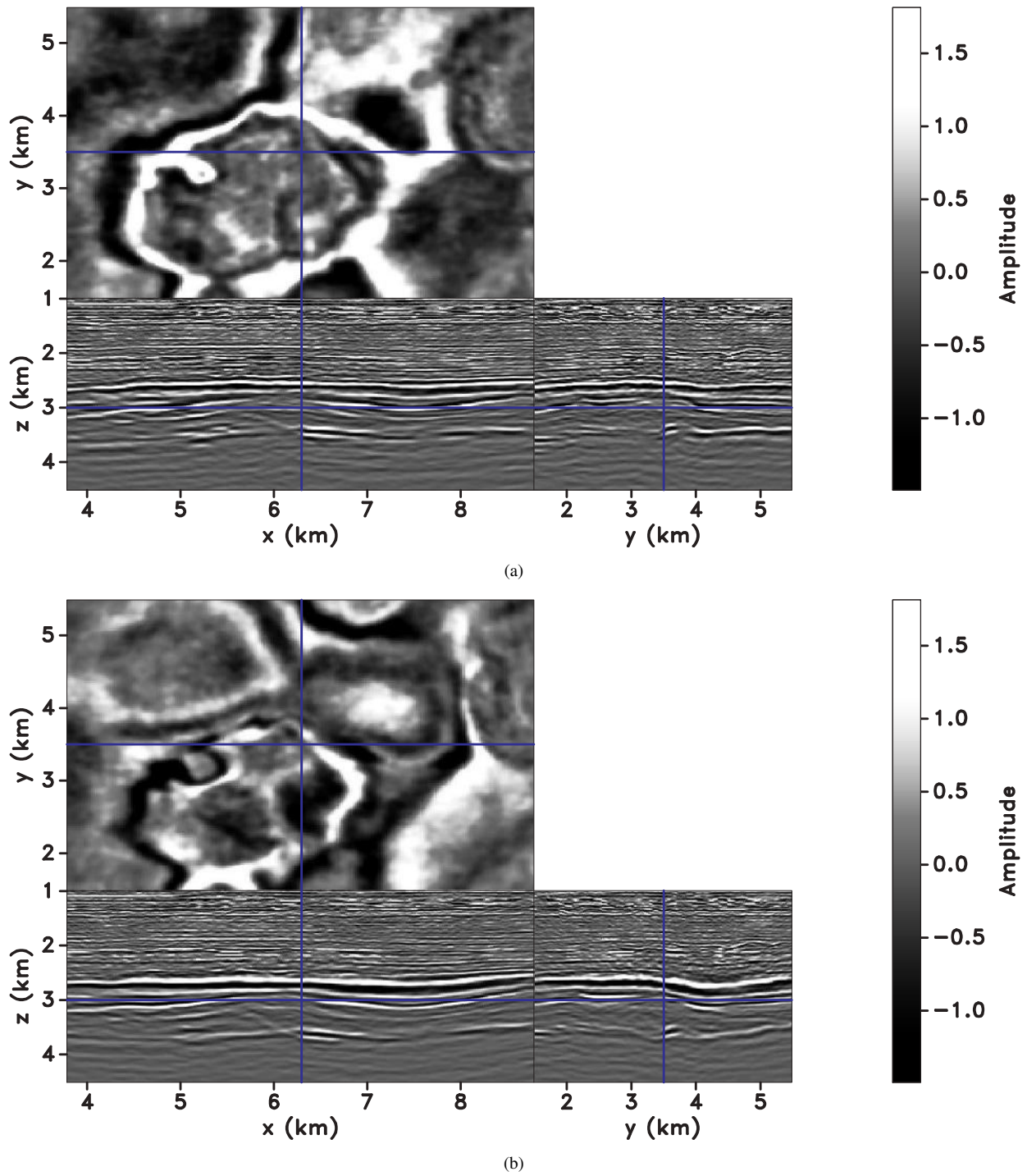


Figure 7. North Sea field data example. (a) The migrated image obtained with the initial model, and (b) the migrated image obtained with the updated model.

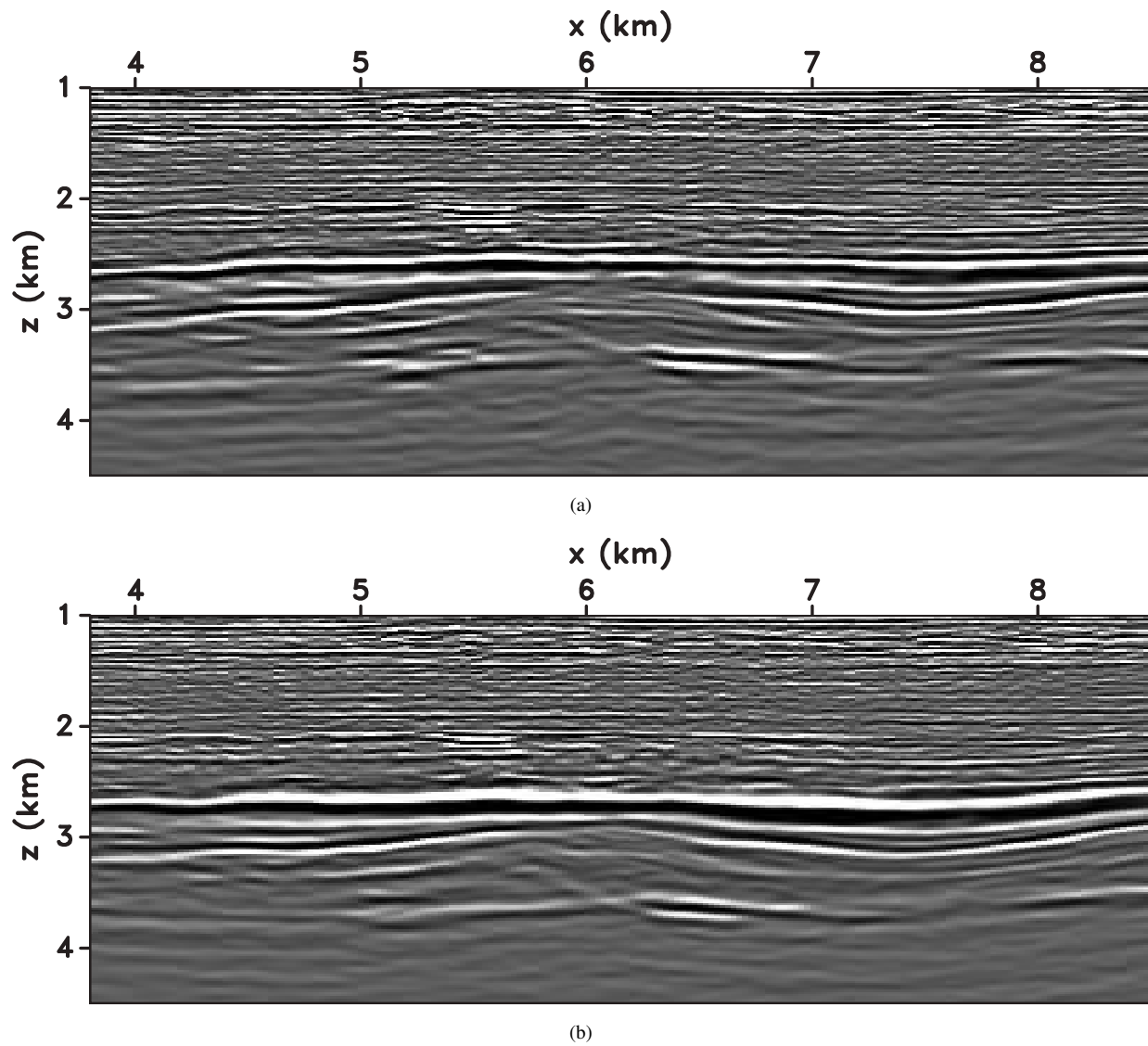


Figure 8. North Sea field data example. Zoom-in image extracted at $y = 3.5$ km to highlight the difference in image quality. (a) The image obtained with the initial model and (b) the image obtained with the updated model.

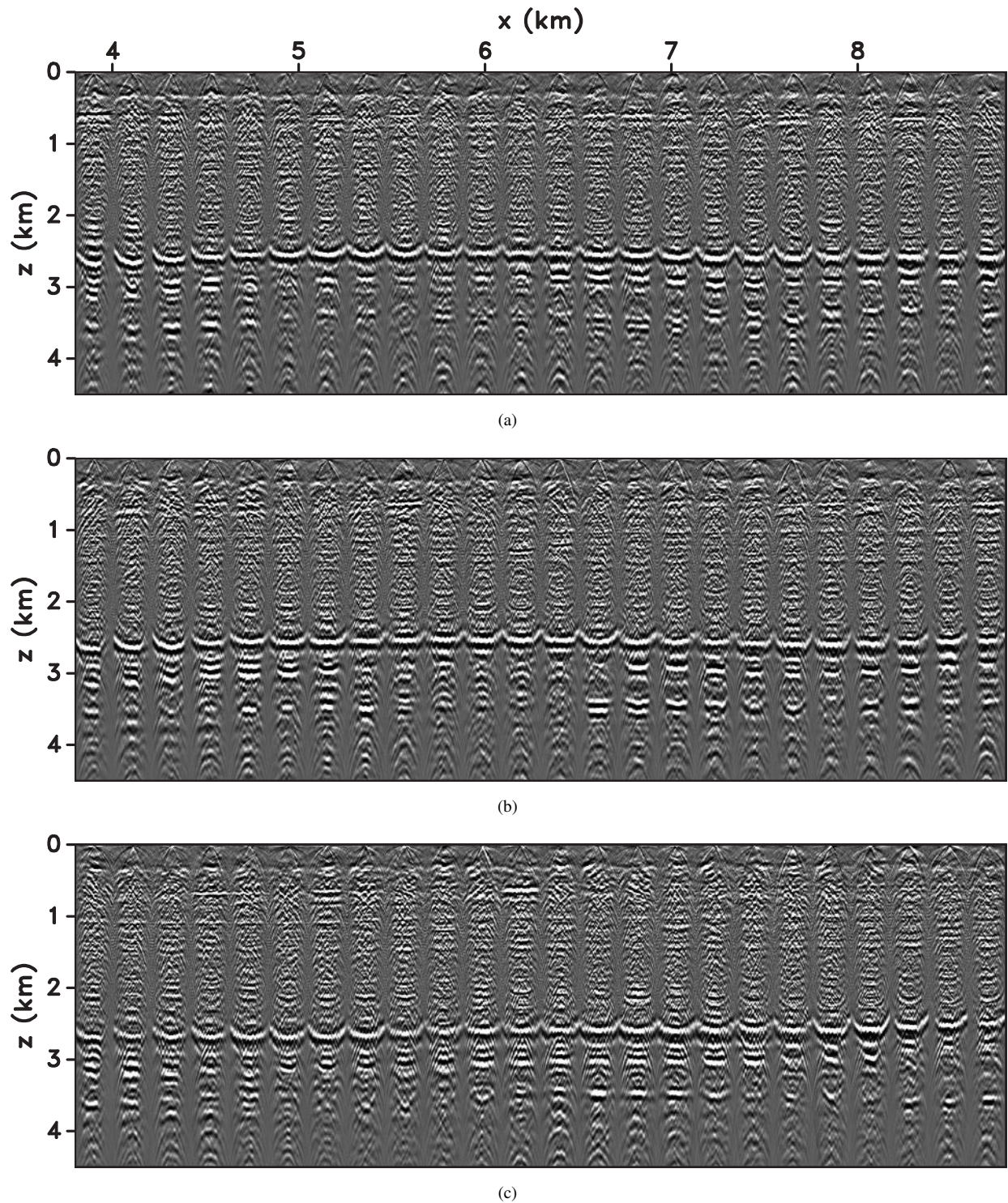


Figure 9. Angle-domain gathers obtained with the initial model at (a) $y = 3$ km, (b) $y = 6$ km, and (c) $y = 9$ km. The angle range is from -60° to 60° .

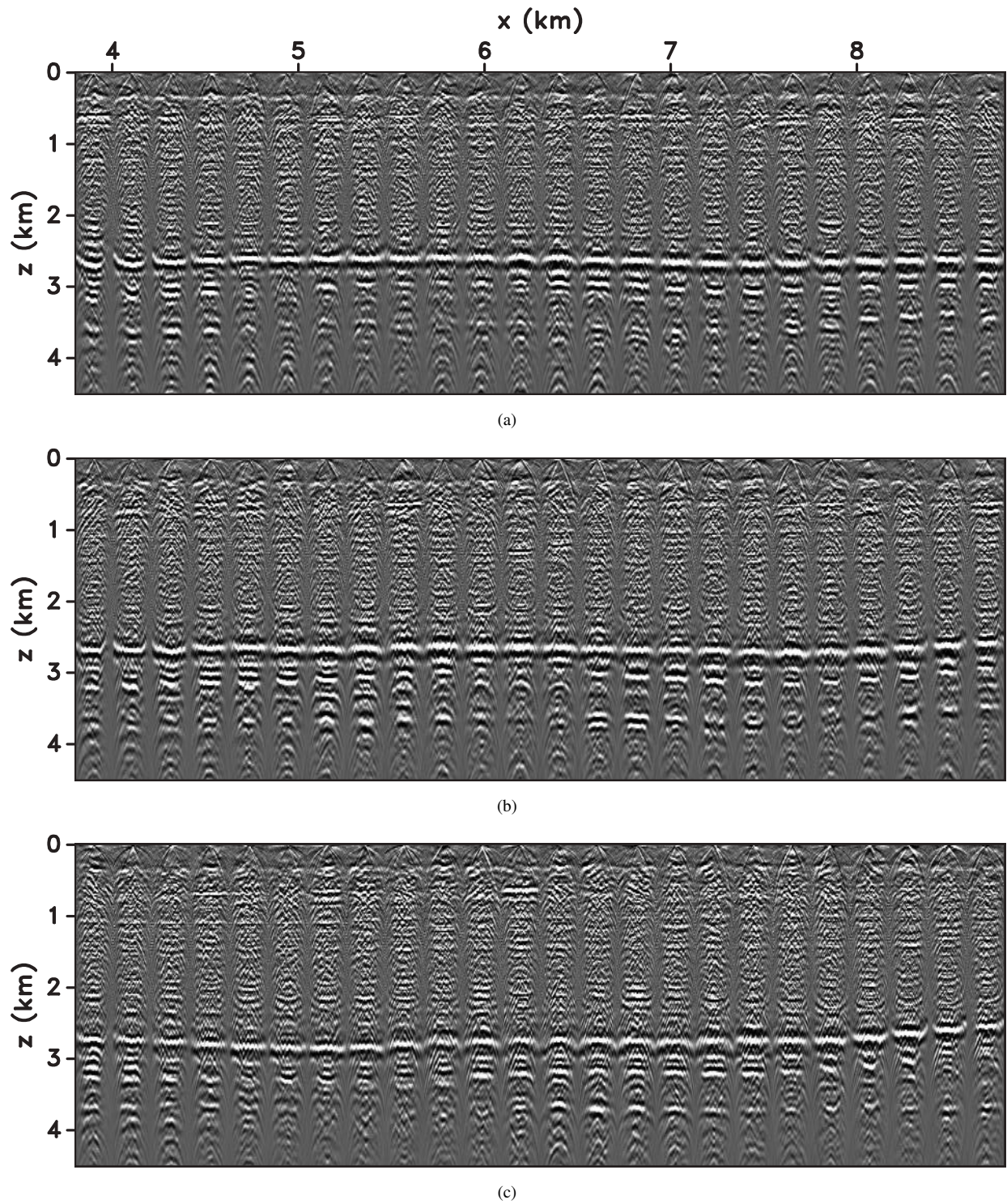


Figure 10. Angle-domain gathers obtained with the updated model at (a) $y = 3$ km, (b) $y = 6$ km, and (c) $y = 9$ km. The angle range is from -60° to 60° .

racy and image quality. In addition, the method is computationally efficient in 3D velocity model building applications.

6 ACKNOWLEDGMENTS

We thank sponsor companies of the Consortium Project on Seismic Inverse Methods for Complex Structures, whose support made this research possible. The authors would also like to thank Statoil ASA and the Volve license partners Exxon-Mobil E&P Norway and Bayerngas Norge, for the release of the Volve data. The reproducible numeric examples in this paper use the Madagascar open-source software package freely available from <http://www.ahay.org>.

7 DISCLAIMER

The views expressed in this paper belong to the authors and do not necessarily reflect the views of Statoil ASA and the Volve field license partners.

REFERENCES

- Al-Yahya, K., 1989, Velocity analysis by iterative profile migration: *Geophysics*, **54**, 718–729.
- Brown, M. P., J. H. Higginbotham, and R. G. Clapp, 2008, Velocity model building with wave equation migration velocity focusing analysis: 78th Annual International Meeting, SEG, Expanded Abstracts, 3078–3082.
- Eggen, J., S. H. Gray, and Y. Zhang, 2009, An overview of depth imaging in exploration geophysics: *Geophysics*, **74**, WCA5–WCA17.
- Faye, J. P., and J. P. Jeannot, 1986, Prestack migration velocities from focusing depth analysis: 56th Annual International Meeting, SEG, Expanded Abstracts, 438–440.
- Higginbotham, J. H., and M. P. Brown, 2008, Wave equation migration velocity focusing analysis: 78th Annual International Meeting, SEG, Expanded Abstracts, 3083–3086.
- Luo, Y., and G. Schuster, 1991, Wave equation traveltime inversion: *Geophysics*, **56**, 645–653.
- Plessix, R.-E., 2006, A review of the adjoint state method for computing the gradient of a functional with geophysical applications: *Geophysical Journal International*, **167**, 495–503.
- , 2009, Three-dimensional frequency-domain full-waveform inversion with an iterative solver: *Geophysics*, **74**, WCC53–WCC61.
- Pratt, R. G., 1999, Seismic waveform inversion in the frequency domain, Part 1: Theory and verification in a physical scale model: *Geophysics*, **64**, 888–901.
- Sava, P., and B. Biondi, 2004, Wave-equation migration velocity analysis - I: Theory: *Geophysical Prospecting*, **52**, 593–606.
- Sava, P., and S. Fomel, 2006, Time-shift imaging condition in seismic migration: *Geophysics*, **71**, S209–S217.
- Shen, P., and W. W. Symes, 2008, Automatic velocity analysis via shot profile migration: *Geophysics*, **73**, VE49–VE59.
- Sirgue, L., and R. Pratt, 2004, Efficient waveform inversion and imaging: A strategy for selecting temporal frequencies: *Geophysics*, **69**, 231–248.
- Symes, W., 2009, Migration velocity analysis and waveform inversion: *Geophysical Prospecting*, **56**, 765–790.
- Szydluk, T., P. Smith, S. Way, L. Aamodt, and C. Friedrich, 2007, 3-d pp/ps prestack depth migration on the volve field: First break, **25**, 43–47.
- Tarantola, A., 1984, Inversion of seismic reflection data in the acoustic approximation: *Geophysics*, **49**, 1259–1266.
- Thomsen, L., 1986, Weak elastic anisotropy: *Geophysics*, **51**, 1954–1966. (Discussion in GEO-53-04-0558-0560 with reply by author).
- van Leeuwen, T., and W. A. Mulder, 2010, A correlation-based misfit criterion for wave-equation traveltime tomography: *Geophysical Journal International*, **182**, 1383–1394.
- Vigh, D., and E. W. Starr, 2008, 3D prestack plane-wave, full-waveform inversion: *Geophysics*, **73**, VE135–VE144.
- Wang, B., Y. Kim, C. Mason, and X. Zeng, 2008, Advances in velocity model-building technology for subsalt imaging: *Geophysics*, **73**, VE173–VE181.
- Wang, B., C. Mason, M. Guo, K. Yoon, J. Cai, J. Ji, and Z. Li, 2009, Subsalt velocity update and composite imaging using reverse-time-migration based delayed-imaging-time scan: *Geophysics*, **74**, WCA159–WCA166.
- Wang, B., F. Qin, V. Dirks, P. Guillaume, F. Audebert, and D. Epili, 2005, 3-d finite angle tomography based on focusing analysis: 78th Annual International Meeting, SEG, Expanded Abstracts, 2546–2549.
- Yang, T., and P. Sava, 2010a, Moveout analysis of wave-equation extended images: *Geophysics*, **75**, S151–S161.
- , 2010b, Wave-equation migration velocity analysis with time-lag imaging: *Geophysical Prospecting*, submitted for publication.
- , 2011, Waveform inversion in the image domain: Presented at the 73th EAGE Conference and Exhibition, Extended Abstracts.
- Yilmaz, O., 2001, *Seismic Data Analysis* (2nd edition): Society of Exploration Geophysicists.
- Zhang, Y., and D. Wang, 2009, Traveltime information-based wave-equation inversion: *Geophysics*, **74**, WCC27–WCC36.

